

## Enhancing wear resistance: In-situ ceramic phase precipitation for strengthening and toughening FeCoNiCrNx high-entropy alloy films

W. Liu<sup>a</sup>, C.T. Wang<sup>b</sup>, S.C. Zhao<sup>a</sup>, L. Chen<sup>a</sup>, Y.T. Li<sup>c</sup>, X. Jiang<sup>a,\*</sup>, Y.X. Leng<sup>a,d</sup>

<sup>a</sup> Key Laboratory of Advanced Technologies of Materials, Ministry of Education, School of Materials Science and Engineering, Southwest Jiaotong University, Chengdu 610031, China

<sup>b</sup> Key Laboratory of Marine Materials and Related Technologies, Zhejiang Key Laboratory of Marine Materials and Protective Technologies, Ningbo Institute of Materials Technology and Engineering, Chinese Academy of Sciences, Ningbo 315201, China

<sup>c</sup> School of Mechanical and Electrical Engineering, Mianyang Teachers' College, Mianyang 621000, China

<sup>d</sup> Sichuan Province International Science and Technology Cooperation Base of Functional Materials, College of Medicine, Southwest Jiaotong University, Chengdu 610031, China



### ARTICLE INFO

#### Keywords:

FeCoCrNi  
High entropy alloy film  
Nanocomposite structure  
Reactive magnetron sputtering  
Wear resistance

### ABSTRACT

FeCoNiCr high-entropy alloys have attracted widespread attention because of their excellent toughness; however, their insufficient hardness limits their application in wear-resistant films. The introduction of non-metallic elements is an effective method for strengthening high entropy alloys films. In this study, high-entropy alloy films of FeCoNiCrNx with varying nitrogen content were fabricated using reactive magnetron sputtering. The influence of nitrogen content on the structure, mechanical properties, and tribological behavior of these high-entropy alloy films was studied. With an increase in nitrogen content, the FeCoNiCrNx film undergoes amorphization and simultaneous precipitation of Cr<sub>2</sub>N phases. At lower nitrogen flow rates (0–4 sccm), the film exhibits lower hardness (8.51–10.97 GPa) and poor wear resistance. At moderate nitrogen flow rates (8 sccm), the film exhibits enhanced hardness (12.8 GPa) and toughness, leading to favorable wear resistance ( $4.04 \times 10^{-6} \text{ mm}^3 \text{ N}^{-1} \text{ m}^{-1}$ ). A further increase in the nitrogen flow rates (12–16 sccm), while raising hardness (13.08–15.17 GPa), leads to a slight reduction in toughness and consequently, a mild decrease in wear resistance ( $4.37\text{--}5.09 \times 10^{-6} \text{ mm}^3 \text{ N}^{-1} \text{ m}^{-1}$ ). A biphase structure design combining FeCoNiCr high entropy alloy and ceramic (Cr<sub>2</sub>N) improved the strength and toughness of FeCoNiCrNx and significantly enhanced its wear resistance, thus enhancing its application potential.

### 1. Introduction

High-entropy alloys (HEAs) are multi-principal component alloys proposed by Yeh [1] and Cantor [2]. HEAs are characterized by high configurational entropy resulting from numerous components, leading to a single solid-solution phase. Recently, researchers have shown that multiphase high-entropy alloys can give materials stronger mechanical properties [3,4]. In addition, Cantor, one of the founders, also pointed out that the multiphase alloy also fits with the high entropy alloy concept [5]. Owing to lattice distortion, hysteresis diffusion, high-entropy, and cocktail effects, HEAs exhibit promising potential for applications requiring high-temperature [6], wear [7], and oxidation resistances [8].

Among the representative HEA systems, FeCoNiCr systems possess relatively low fault energy (13 mJ/m<sup>2</sup> at 77 K) [9], which is lower than

that of stainless steel (25.52 mJ/m<sup>2</sup>) [10]. Consequently, at low temperatures (77 K), the deformation mode of the FeCoNiCr alloy changed from dislocation slip at 293 K to a combination of dislocation slip and twinning. Although FeCoNiCr demonstrated attractive low-temperature properties with a high elongation of 55 %, it also suffered from significant drawbacks such as low strength (480 and 260 MPa at 77 and 293 K, respectively) [9], which limits its application in the field of friction.

To enhance the applicability of FeCoNiCr alloys, numerous modifications have been made, primarily focusing on the induction of a secondary phase through element doping. This can be categorized into metallic and non-metallic element doping. In the case of metallic element doping, the addition of larger atomic-sized elements such as Al leads to significant lattice distortion. This results in instability of the original face-centered cubic (FCC) phase, promoting the precipitation of the body-centered cubic (BCC) phase, which contributes to an increase

\* Corresponding author.

E-mail address: [jiangxin@swjtu.edu.cn](mailto:jiangxin@swjtu.edu.cn) (X. Jiang).

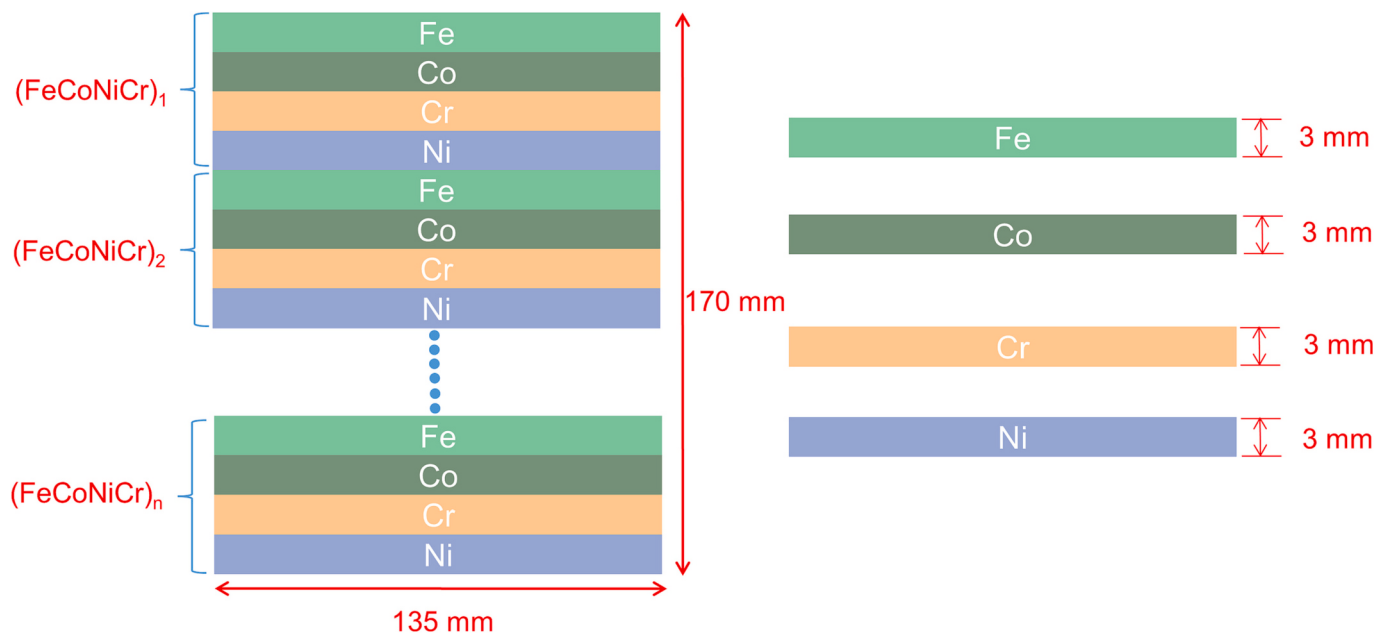


Fig. 1. Schematic diagram of the spliced target.

in strength, as documented in references [11, 12]. Similarly, the introduction of elements like Ti [13] and Nb [14] has led to the precipitation of a secondary phase within the alloy, enhancing mechanical properties at the expense of plasticity. The incorporation of Mo into CoCrFeNi alloys induces the precipitation of Mo-rich sigma phases, resulting in increased hardness and a reduction in wear rate from  $3.6 \times 10^{-4} \text{ mm}^3 \text{ N}^{-1} \text{ m}^{-1}$  to  $1.8 \times 10^{-4} \text{ mm}^3 \text{ N}^{-1} \text{ m}^{-1}$  [15]. On the other hand, doping with non-metallic elements, such as carbon, facilitates the precipitation of carbides in FeCoNiCr, leading to increased hardness and improved wear resistance. However, an excessive carbon content can result in a substantial precipitation of carbides, which diminishes toughness and wear resistance [16]. Conversely, the introduction of interstitial nitrogen has been found to increase the yield strength and elongation of FeCoNiCr alloys from 520 MPa and 27 % to 650 MPa and 34 %, respectively [17]. This enhancement breaks the strength-ductility trade-off, making nitrogen doping a promising avenue for augmenting wear resistance.

The incorporation of coatings or films on the surface of structural materials can bestow new surface properties to the materials, achieving the performance required by their working conditions and extending their service life. Presently, for FeCoNiCr-based coatings, the focus is predominantly on enhancing the tribological properties through the introduction of ceramic phases via laser cladding technology. For example, by embedding TiC into the FeCoNiCr matrix, the hardness has been increased from 340 HV to 420 HV, and the wear rate has been reduced from 0.09 to 0.05  $\text{mm}^3 \text{ N}^{-1} \text{ m}^{-1}$  [18]. Additionally, the incorporation of  $\text{Ti}_x\text{B}_{2x}$  has resulted in a reduction of the wear track width in CoCrFeNi from 0.693 mm to 0.466 mm [19].

The doping of ceramic phases has been widely validated to enhance the wear resistance of HEA coatings or films. However, compared with the doped ceramic phases, in-situ precipitation may yield superior toughness, promising a synergistic combination of strength and toughness to further augment wear resistance. Reactive magnetron sputtering facilitates the in-situ precipitation of ceramic phases by introducing reactive gases during the deposition process. Additionally, the rapid quenching effect inherent to magnetron sputtering facilitates the formation of films with a fine-grained microstructure. This refinement in grain size contributes to a significant increase in hardness, which can reach 3 to 4 times that of the corresponding bulk material [20,21]. Based on these insights, nitrogen was introduced into FeCoNiCr films through

**Table 1**  
Deposition parameters.

Ar flow rate (scm)	Voltage-pulse width-frequency (V·μs·Hz)	Bias (V)	Deposition time (min)	N <sub>2</sub> flow rate (sccm)
40	800–150–200	-50	50	0, 4, 8, 12, 16

reactive magnetron sputtering, which combined with the nitrogen-reactive elements (Cr) to form Me—N bonds, thereby improving the film hardness. Furthermore, the unreacted Cr and weak-reactive metals, such as Fe, Co, Ni, increase toughness of the film through Me—Me metal bonds, thereby achieving a “strength and toughness integrated” structural design. The effects of nitrogen content on the microstructure, mechanical properties, and tribological properties of FeCoNiCr HEA films were studied.

## 2. Experiments

### 2.1. Film deposition

The FeCoNiCrN<sub>x</sub> films were prepared using the unbalanced magnetron sputtering system (UBMS450, Sky Technology Development Co. Ltd., China) at various nitrogen flow rates. The high power pulse power supply (HPP12S1, Chengdu Zhongxinda, China) was connected to the target. The FeCoNiCr target consists of pure metal bars of Fe ( $\geq 99.9\%$ ), Co ( $\geq 99.9\%$ ), Ni ( $\geq 99.9\%$ ), and Cr ( $\geq 99.9\%$ ). The stitching methods employed are denoted as  $(\text{Co—Ni—Fe—Cr})_1$ ,  $(\text{Co—Ni—Fe—Cr})_2$ ,  $(\text{Co—Ni—Fe—Cr})_3$ , ...,  $(\text{Co—Ni—Fe—Cr})_n$ . The schematic diagram of the target bonding is shown in Fig. 1. Before deposition, a 304 stainless steel substrate was cleaned with acetone and anhydrous ethanol to eliminate surface impurities. The base pressure of the chamber was  $2.0 \times 10^{-3} \text{ Pa}$ . The distance between target and substrate was set to 80 mm. First, a DC power supply was utilized for a 10-min cleaning process to remove impurities on the target surface. Subsequently, a -1500 V bias was applied for 20 min to clean the substrate and eliminate the impurities on it. The deposition parameters are listed in Table 1.

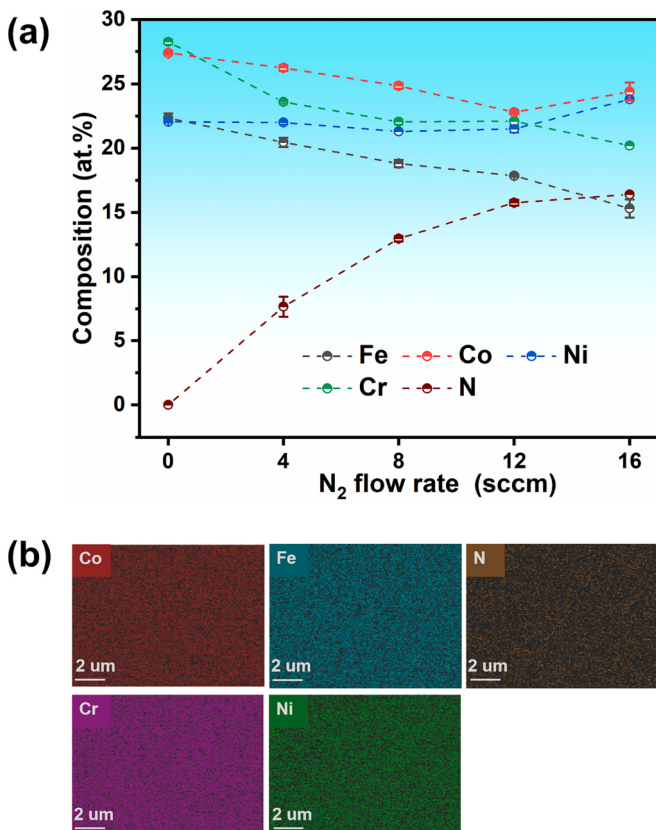


**Fig. 2.** (a) Elemental composition of the films under different nitrogen flow rates. (b) Surface composition distribution map of the film deposited at a nitrogen flow rate of 16 sccm.

## 2.2. Characterization

The surface and sectional morphologies of the films were observed using scanning electron microscopy (SEM) (JSM-7800 F-Japan). The chemical compositions of the films were characterized using energy-dispersive X-ray spectroscopy (EDS) in conjunction with SEM. The phase analysis of the film was performed via X-ray diffraction (XRD) (GIXRD, Rigaku Smart Lab, Japan). X-ray photoelectron spectroscopy (XPS) (Thermo Fisher Scientific K-Alpha), with C1s (284.8 eV) as the calibration reference, was employed to analyze the surface elemental composition and valence state of the film. Planar samples for transmission electron microscopy (TEM) were prepared using an ion thinning equipment (PIPS II 695, Gatan), and the TEM data was captured using a field-emission transmission electron microscope (JEM-2100F, Japan). The residual stress of the film was determined using a wafer curvature method and calculated using a modified Stoney equation [22]:

$$\sigma_r = \frac{Et_s^2}{6(1-v)t} * \left( \frac{1}{R_f} - \frac{1}{R_o} \right) \quad (1)$$

where E is Young's modulus, t is the wafer thickness, t<sub>s</sub> is the film thickness, v is Poisson's ratio (v = 0.279), R<sub>f</sub> is the final radius of the curvature and R<sub>o</sub> is the initial radius of curvature.

The indentation morphology of the films deposited on the silicon wafer was characterized using a Vickers hardness tester and scanning electron microscope (JSM-7800 F-Japan) under a load of 10 N, to analyze the toughness of the films. A nanoindenter (G200, USA) was used to measure the nanoindentation hardness of the films. The indenter was a regular diamond quadrangular cone with an opposite angle of 136°, and its tip had a radius of curvature of 20 nm. Continuous stiffness measurements were performed. The tribological properties of the FeCoNiCrN<sub>x</sub> films in a dry atmosphere at 298 K were studied using a

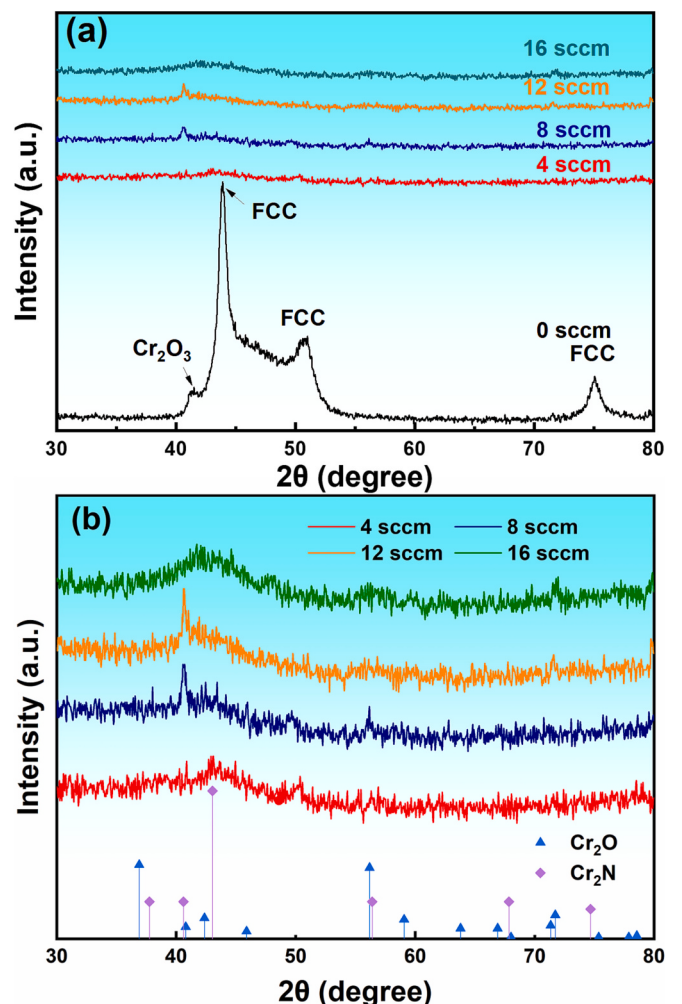


**Fig. 3.** XRD pattern of the film at different nitrogen flow rates: (a) 0, 4, 8, 12, and 16 sccm and (b) 4, 8, 12, and 16 sccm.

tribometer (CSM, Switzerland) in the reciprocating mode. The sliding velocity, applied load, and frequency were kept constant at 1.885 cm·s<sup>-1</sup>, 2 N, and 3 Hz, respectively. Al<sub>2</sub>O<sub>3</sub> balls with diameters of 6 mm were used as grinding pairs. The friction coefficient was continuously recorded using a friction meter. The wear rate (K) was calculated using the following formula:

$$K = V / (F \times d) \quad (2)$$

where V represents the wear volume, determined using a white-light interferometer (Contour GT, Bruker); F is the applied load; and d is the total sliding distance.

## 3. Results and discussion

### 3.1. Composition of the films

**Fig. 2(a)** shows the chemical compositions of the films at different nitrogen flow rates. With increasing nitrogen flow rate, the nitrogen content gradually increased and reached a stable level at 12 sccm, whereas the metallic element content gradually decreased. The metallic elements in the film were within the range defined for HEAs (5–35 %). Surface EDS scanning of the 16 sccm film reveals a uniform distribution of all elements without any compositional segregation.

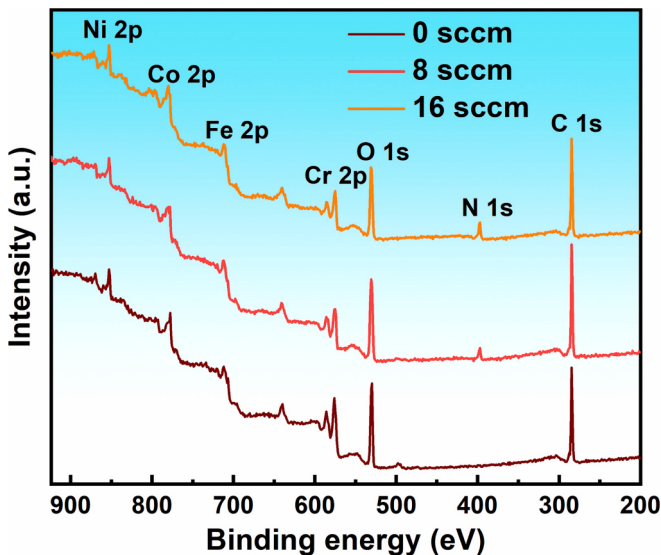


**Fig. 4.** XPS survey spectra of the films deposited at various nitrogen flow rates (0, 8, and 16 sccm).

### 3.2. Film crystallization

Fig. 3 shows the XRD patterns of films prepared at different nitrogen flow rates. Compared to the nitrogen-treated films, the 0 sccm film exhibits better crystallinity, with diffraction peaks at  $41.5^\circ$ ,  $43.9^\circ$ ,  $50.6^\circ$ , and  $75.1^\circ$  (Fig. 3(a)). The peaks at  $43.9^\circ$ ,  $50.6^\circ$ , and  $75.1^\circ$  correspond to the FCC phase, as reported in the literature [23]. However, the peak at  $41.5^\circ$  appears as a broad peak, which has not been previously reported for FeCoNiCr. Thus, it is inferred that this peak is not associated with FeCoNiCr but rather corresponds to  $\text{Cr}_2\text{O}_3$  (PDF#38-1479). After the introduction of nitrogen, the crystallinity of the film deteriorated. To precisely determine the phase composition of the films, the XRD spectrum of the 0 sccm film was subtracted, as shown in Fig. 3(b).

As shown in Fig. 3(b), upon the addition of nitrogen atoms, the XRD spectra not only displayed diffraction peaks of  $\text{Cr}_2\text{O}$  (PDF#43-1040), but also manifested peaks indicative of  $\text{Cr}_2\text{N}$ , signifying the successful incorporation of nitrogen. The transformation of  $\text{Cr}_2\text{O}_3$  into  $\text{Cr}_2\text{O}$  was attributed to the introduction of nitrogen atoms, which diluted the oxygen content and decreased the Cr:O ratio. Previous reports on bulk FeMnCoCr HEAs revealed the precipitation of  $\text{Cr}_2\text{N}$  after the introduction of only 2.6 at.% of nitrogen, as evidenced by TEM [24]. This demonstrates the favorable reactivity between Cr and N among the four metallic elements. Additionally, other studies on bulk CoCrFeMnNi HEAs have indicated that a small amount of N doping (0.94 at.%) can

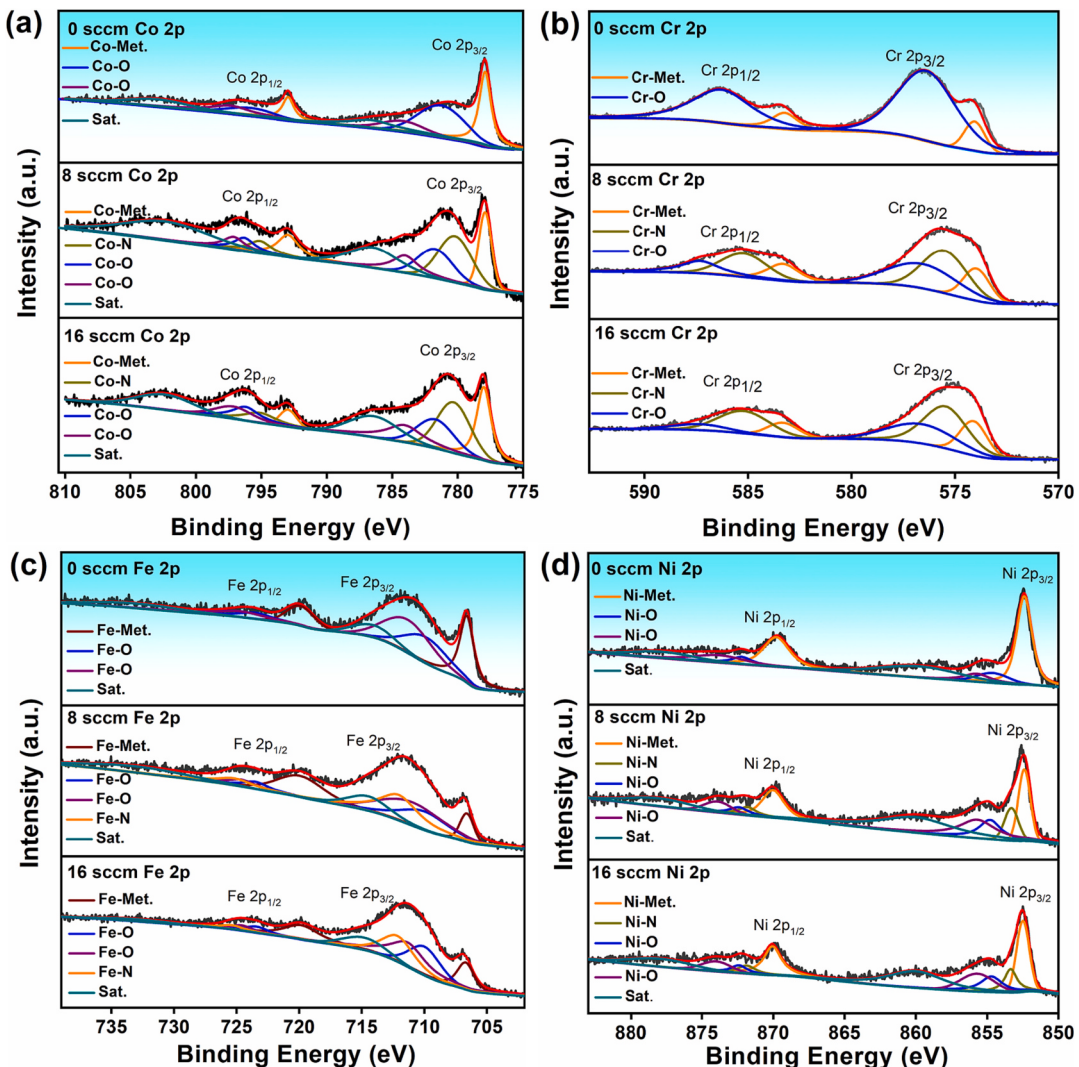


**Fig. 5.** High-resolution XPS spectra and fitting results of FeCoNiCr films at different nitrogen flow rates.

**Table 2**

Peak areas of Cr-Met., oxide, and nitride states in the XPS-Cr spectrum.

Sample	0 sccm	8 sccm	16 sccm
Cr-Met. peak area (cps-eV)	22,165.38	12,201.25	14,809.62
Chromium oxide peak area (cps-eV)	63,681.09	31,379.75	18,773.82
Chromium nitride ( $\text{Cr}_2\text{N}$ ) peak area (cps-eV)	/	16,783.62	18,084.58
Proportion of nitride peak area in Cr element	/	27.8 %	35 %

form the  $\text{Cr}_2\text{N}$  phase and that the precipitated phase exhibits a semi-coherent relationship with the FCC matrix:  $\text{FCC}\langle 111 \rangle \parallel \text{Cr}_2\text{N}\langle 0001 \rangle$  and  $\text{FCC}\langle 110 \rangle \parallel \text{Cr}_2\text{N}\langle \bar{1}\bar{1}00 \rangle$  [25]. In the CoCrNi system, a low nitrogen content results in the formation of  $\text{Cr}_2\text{N}$  rather than  $\text{CrN}$  owing to the lower Gibbs free energy of formation [26]. When the nitrogen flow rate reaches 16 sccm, the film becomes amorphous. This is attributed to the two types of metallic elements in the film. One type is reactive with nitrogen, such as Cr, whereas the other type, including Fe, Co, and Ni, exhibits limited reactivity towards nitrogen. When the nitrogen content was low, a sufficient number of reactive elements combined with nitrogen to form crystalline nitrides. However, as the nitrogen content was further increased, no adequate reactive elements were available for matching, and the introduction of excessive nitrogen caused a significant distortion in the original crystalline lattice. When the distortion became significant, the film adopted an amorphous structure to minimize its energy.

### 3.3. Chemical states of the elements in the films

Fig. 4 shows the XPS survey spectra of the films deposited at various nitrogen flow rates. The nitrogen content on the film surface increased with increasing nitrogen flow rate. In addition to the four metallic elements (Fe, Co, Ni, and Cr), adsorbed oxygen and carbon were present.

Fig. 5 shows the XPS fitting results for the four metallic elements, Fe, Co, Ni, and Cr. In the spectrum of Cr, all samples exhibited Cr-Met. (574.03 eV [27]) and Cr—O (576.61 eV) peaks at the  $2p_{3/2}$  orbital, while the nitrogen-containing film showed an additional Cr—N ( $\text{Cr}_2\text{N}$  575.26 eV [28]) peak. In the spectrum of Co, all samples exhibit Co-Met. (777.9 eV) [26] and Co—O (780.2 and 784.2 eV) [29] peaks at the  $2p_{3/2}$  orbital, and the nitrogen-containing film displays an extra Co—N (781.7 eV) peak [30]. Similarly, in the spectrum of Fe, all samples displayed Fe-Met. (706.8 eV) and Fe—O (710 and 711.2 eV) [27] peaks at the  $2p_{3/2}$  orbital, with the nitrogen-containing film showing an additional Fe—N (711.8 eV) [31] peak. In the Ni spectrum, all samples featured Ni-Met. (852.4 eV) and Ni—O (855.7 eV) peaks at the  $2p_{3/2}$  orbital, and the nitrogen-containing film exhibited an additional Ni—N (853.3 eV) peak [32]. These findings indicate that all metallic elements exhibit similar characteristics in the films. In the absence of nitrogen, the metal atoms existed in their elemental or oxidized states, whereas the introduction of nitrogen led to the formation of nitrides.

Table 2. presents the proportions of metals, oxides, and nitrides in the XPS spectra of Cr at different nitrogen flow rates. As the nitrogen flow rate increased, the nitrogen content increased, leading to an increase in the  $\text{Cr}_2\text{N}$  ceramic phase.

### 3.4. Microstructures

Fig. 6(a) shows that the 0 sccm film is primarily composed of the FCC phase. High-resolution imaging revealed distinct lattice fringes with a lattice spacing of  $d = 2.07 \text{ nm}$ , corresponding to the FCC (111) crystal planes. Electron diffraction confirmed the presence of the FCC phase. In addition to the FCC, a small fraction of amorphous phase was present because film deposition under relatively low-temperature conditions results in rapid cooling and limited atomic diffusion, which facilitate the formation of the amorphous phase. Upon introducing an 8 sccm nitrogen flow, the structure of film undergoes a transition from the “FCC +

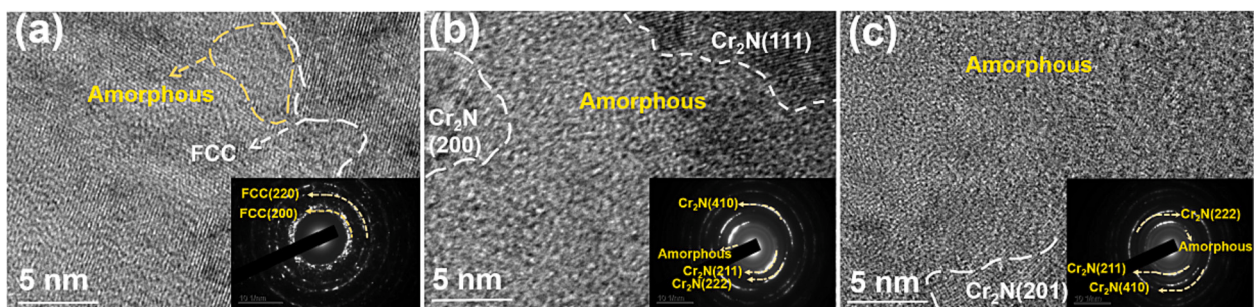


Fig. 6. TEM images and electron diffraction pattern of the films at different nitrogen flows: (a) 0, (b) 8, and (c) 16 sccm.

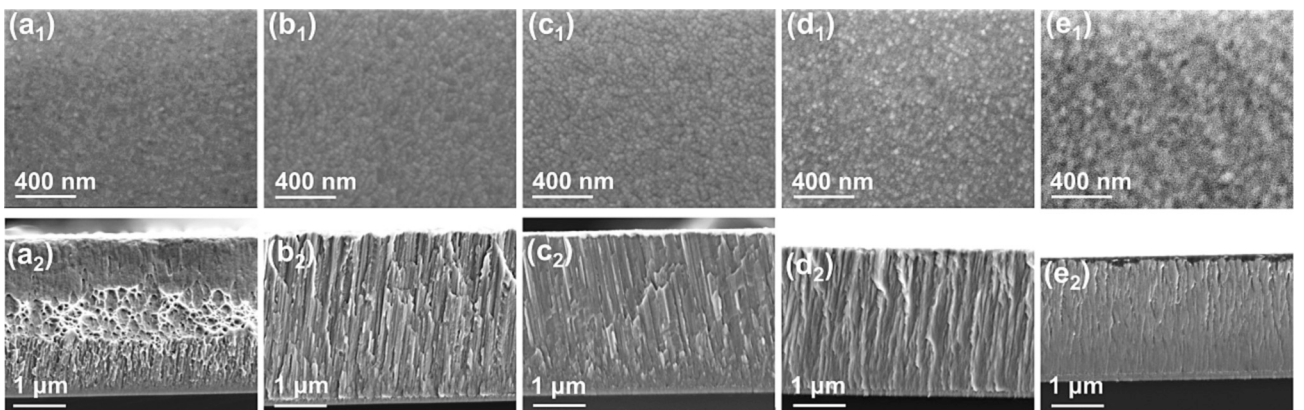
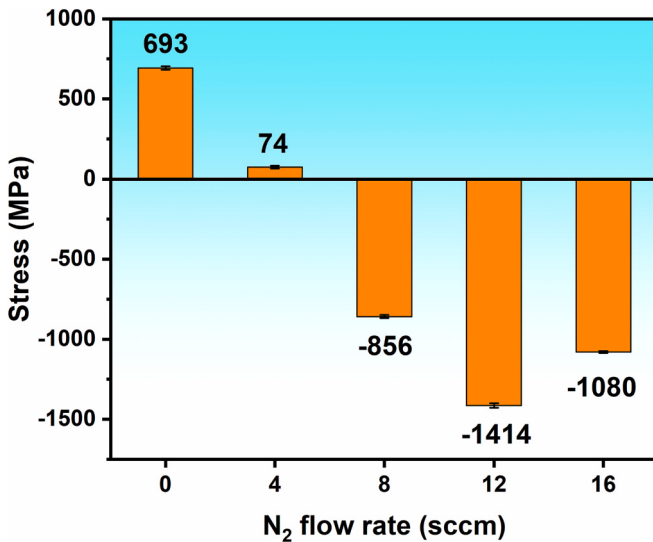


Fig. 7. Surface and section morphologies of the films under different nitrogen flow rates: (a) 0, (b) 4, (c) 8, (d) 12, and (e) 16 sccm.



**Fig. 8.** Residual stress values of the film at different nitrogen flow rates.

amorphous” to “Cr<sub>2</sub>N + amorphous” structure. Further increasing the nitrogen gas flow to 16 sccm maintains the “Cr<sub>2</sub>N + amorphous”, but the lattice fringes of Cr<sub>2</sub>N become indistinct, indicating a reduction in crystallinity, consistent with the XRD results.

The structural transformation of the film after nitrogen introduction can be explained as follows. According to reference [33], the mixing enthalpies of N with Cr, Fe, Co, and Ni are -107, -87, -75, and -69 kJ/mol, respectively. Namely, the film consists of reactive elements (Cr) and weak-reactive elements (Fe, Co, and Ni). The reactive elements react with nitrogen to form stable nitrides (Cr<sub>2</sub>N), whereas the weak-reactive elements react with nitrogen to form unstable nitrides (Fe—N, Ni—N, and Co—N). Electron diffraction and XRD analyses did not detect the nitrides formed by the weak-reactive elements, suggesting that these nitrides exist in an amorphous state. Notably, the solubility of nitrogen in weak-reactive elements is limited, and the nitrogen content is insufficient to react with all metal elements, resulting in the presence of an amorphous structure within the film. Both XRD and TEM results revealed that the film underwent amorphization at higher nitrogen contents, similar to previous studies [34].

**Fig. 7** shows the surface and cross-sectional topographies of the film under different nitrogen flows. **Fig. 7** reveals the formation of nanoscale particle clusters on the film surfaces. The surface morphology of the film deposited at 8 sccm exhibits densely packed clusters. In the cross-sectional view, the film deposited at 0 sccm exhibits a stratified

structure, characterized by a columnar structure near the substrate, an equiaxed crystal morphology in the middle, and a featureless structure at the top. The film thickness was 2.9 μm. Upon the introduction of nitrogen atoms, the structure transformed into a columnar structure. With an increase in the nitrogen gas flow rate, the film thickness gradually decreased to 3.1, 2.8, 2.6, and 2.3 μm, owing to the “target poisoning” effect [35].

### 3.5. Mechanical properties

**Fig. 8** shows the residual stresses of films deposited at different nitrogen flow rates. With an increase in the nitrogen flow rate, the stress in the film gradually transitioned from tensile to compressive. The film, which was initially subjected to a tensile stress of 693 MPa at 0 sccm, was subjected to a maximum compressive stress of 1414 MPa at 12 sccm. At 16 sccm, the compressive stress decreased to 1080 MPa. The ceramic phase was formed upon the incorporation of nitrogen into the metal film. Metals have a higher coefficient of thermal expansion than ceramics. During cooling, under the influence of thermal stress, the metal film contracts more than the Si substrate, resulting in tensile stress. However, with an increase in the nitrogen flow rate, the nitrogen solid solution in the lattice caused lattice expansion, leading to a transition from tensile to compressive stress. The decrease in compressive stress at 16 sccm was attributed to a slight target poisoning due to the excessive nitrogen flow. This resulted in a reduced target power and decreased ion bombardment, leading to a reduction in compressive stress. This phenomenon has been confirmed in previous studies [35].

**Fig. 9** shows the indentation topographies of the films under different nitrogen flow rates. Micro-Vickers hardness tests were conducted on the films deposited on Si substrates under different nitrogen flow rates, at a load of 10 N. Three types of indentation morphologies were observed. The 0 sccm film remained in a metallic state. Despite its higher ductility, the film hardness was insufficient to resist a large load of 10 N, leading to the deformation and the circumferential cracks were observed on the lower right side of the indent. When nitrogen was introduced at optimal flow rates (4 and 8 sccm), the film hardness significantly increased, while a substantial number of Me—Me bonds was retained, which provides ductility to the film. This combination of high hardness and good ductility enhances toughness, preventing the appearance of radial or circumferential cracks under a 10 N load and resulting in the film exhibiting the best indentation toughness. As the nitrogen content increased, the film hardness continued to increase, resulting in a significant reduction in the indentation area. However, the formation of more Me—N bonds reduced the ductility, leading to the formation of radial cracks.

Improving the toughness of hard films is essential for their

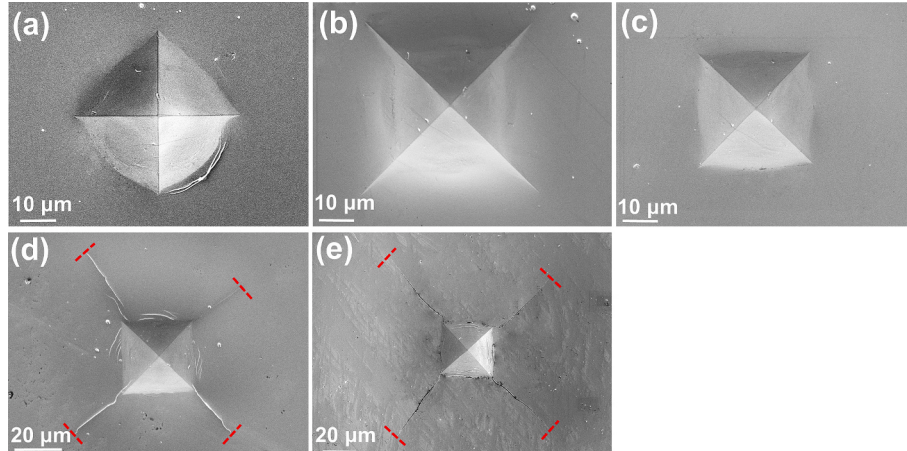


**Fig. 9.** Indentation morphologies of the films subjected to a load of 10 N, under different nitrogen flow rates of (a) 0, (b) 4, (c) 8, (d) 12, and (e) 16 sccm.

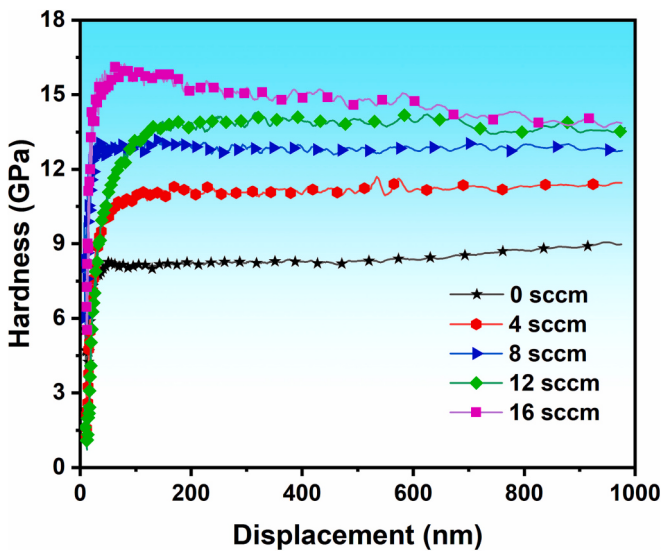


Fig. 10. Film hardness with pressing depth at different nitrogen flow rates.

**Table 3**  
Hardness and elastic modulus of the film under different nitrogen flow rates.

Material	0 sccm	4 sccm	8 sccm	12 sccm	16 sccm
Hardness (GPa)	8.51 ± 0.8	10.97 ± 0.4	12.80 ± 0.6	13.08 ± 0.7	15.17 ± 1.1
Indentation modulus (GPa)	215.40 ± 7.2	227.68 ± 6.8	222.15 ± 6.1	212.98 ± 1.3	220.35 ± 6.8
Crack length (μm)	/	/	/	50.96 ± 3.3	69.69 ± 4.0
K <sub>IC</sub> (MPa·m <sup>1/2</sup> )	/	/	/	1.72 ± 0.2	1.05 ± 0.1

application under harsh friction conditions. Enhancing the toughness involves addressing crack initiation and propagation issues. Compared to crack propagation prevention, inhibiting crack initiation is more challenging because cracks often originate from weak points such as impurities, defects, and brittle phases. During material processing and service, the generation of weak points such as impurities and defects, which lead to crack initiation, is inevitable. Thus, the prevention of crack propagation is more feasible. In this study, the 8 sccm film exhibited excellent fracture toughness, owing to the presence of a nanocomposite structure that significantly impeded crack propagation [36].

Fig. 10 depicts the hardness of the films under different nitrogen flow rates. The hardness of the FeCoNiCrN<sub>x</sub> film was determined using a continuous-stiffness method. The reported hardness values in the Table 3. represent the average of six measurements, excluding the highest and lowest values. The hardness of the films was determined by measuring the hardness at an indentation depth equivalent to one-tenth of the film thickness. Notably, the substrate did not significantly influence the film hardness. As the nitrogen gas flow rate increased, the hardness of the films increased gradually. At a nitrogen flow rate of 16 sccm, the hardness was nearly double that of the film without nitrogen flow (0 sccm). This increase in hardness can be attributed to two factors. First, an increase in the nitrogen content plays a crucial role. Nitrogen combines with the metallic elements and forms a ceramic phase known as Cr<sub>2</sub>N, which significantly enhances the film hardness. Second, TEM observations revealed a composite structure consisting of amorphous and nanocrystalline phases. The presence of abundant phase boundaries impedes the motion of dislocations, contributing to an overall enhancement in the hardness [37].

### 3.6. Tribological properties

Figs. 11 and 12 show the morphology and mapping of the wear marks of the films deposited under different nitrogen flow rates, respectively. Observing the morphology of the wear tracks of the 0 sccm film reveals evident adhesion phenomena, indicating the presence of adhesive wear mechanisms. Both 0 and 4 sccm films exhibit pronounced

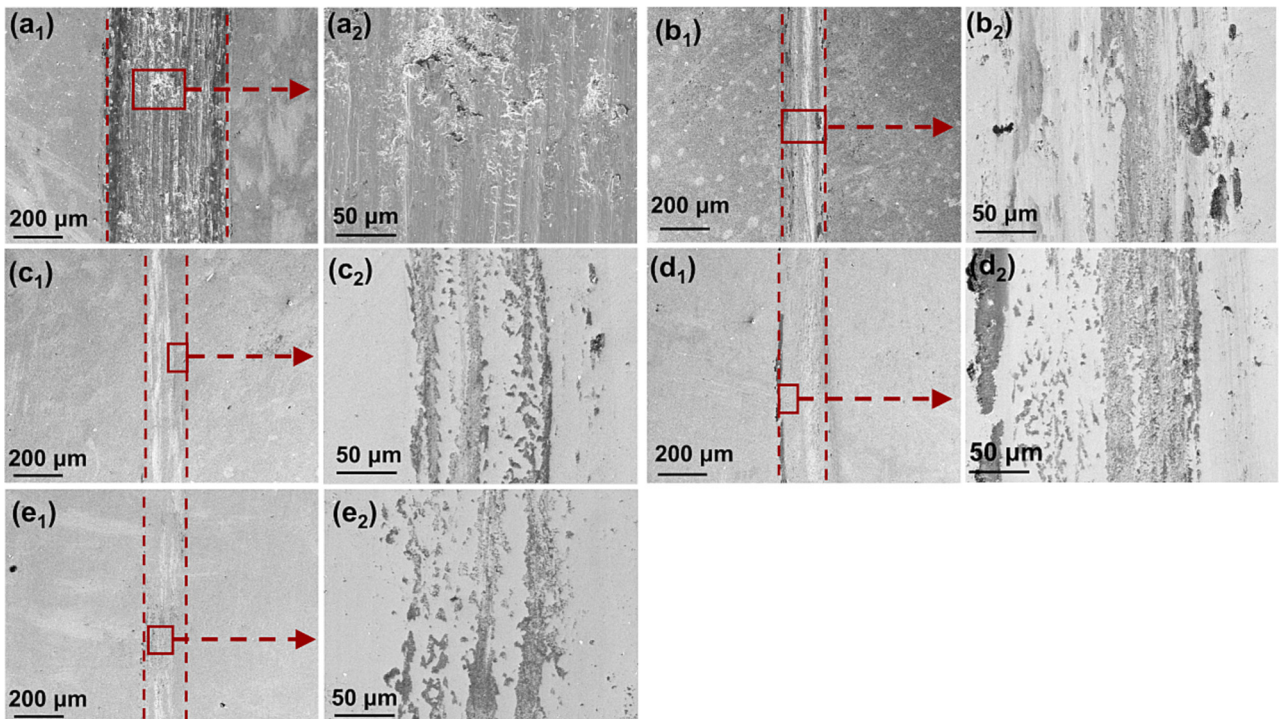
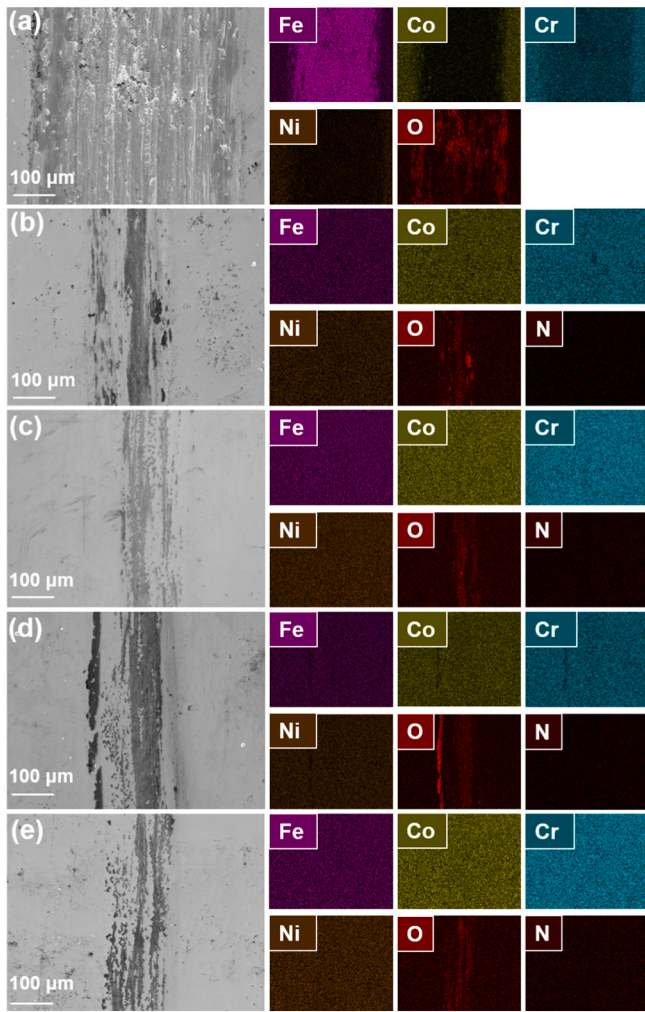


Fig. 11. Wear morphology of the films at different nitrogen flow rates: (a) 0, (b) 4, (c) 8, (d) 12, and (e) 16 sccm.



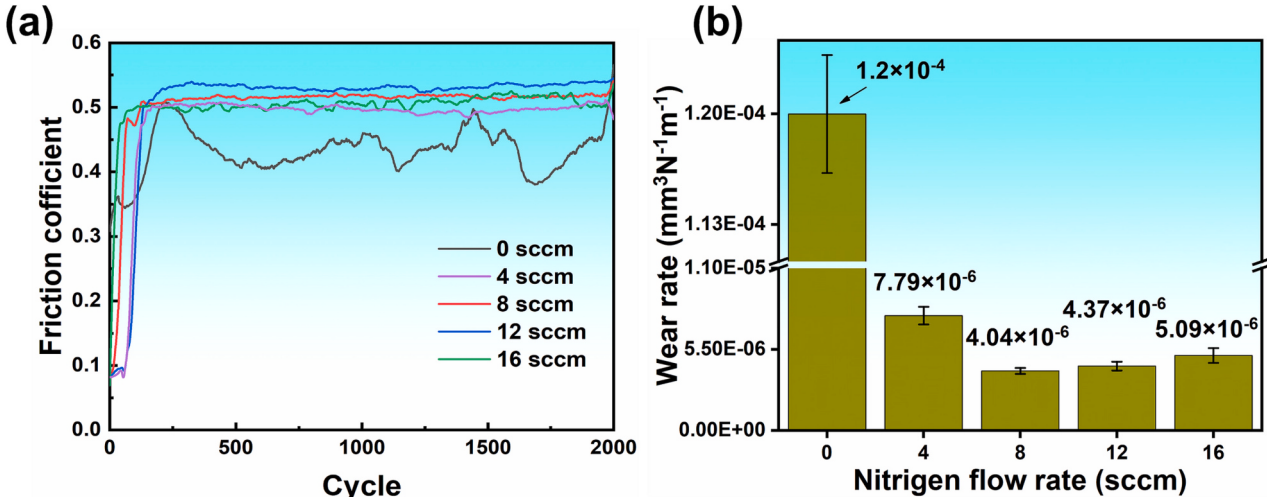
**Fig. 12.** Mapping of film wear marks at different nitrogen flows: (a) 0, (b) 4, (c) 8, (d) 12, and (e) 16 sccm.

plowing grooves, with the 0 sccm film showing more prominent plowing grooves. The occurrence of plowing grooves indicates the presence of abrasive wear mechanisms, which are typically observed when a harder material cuts into a softer material. In comparison, the 0 sccm film

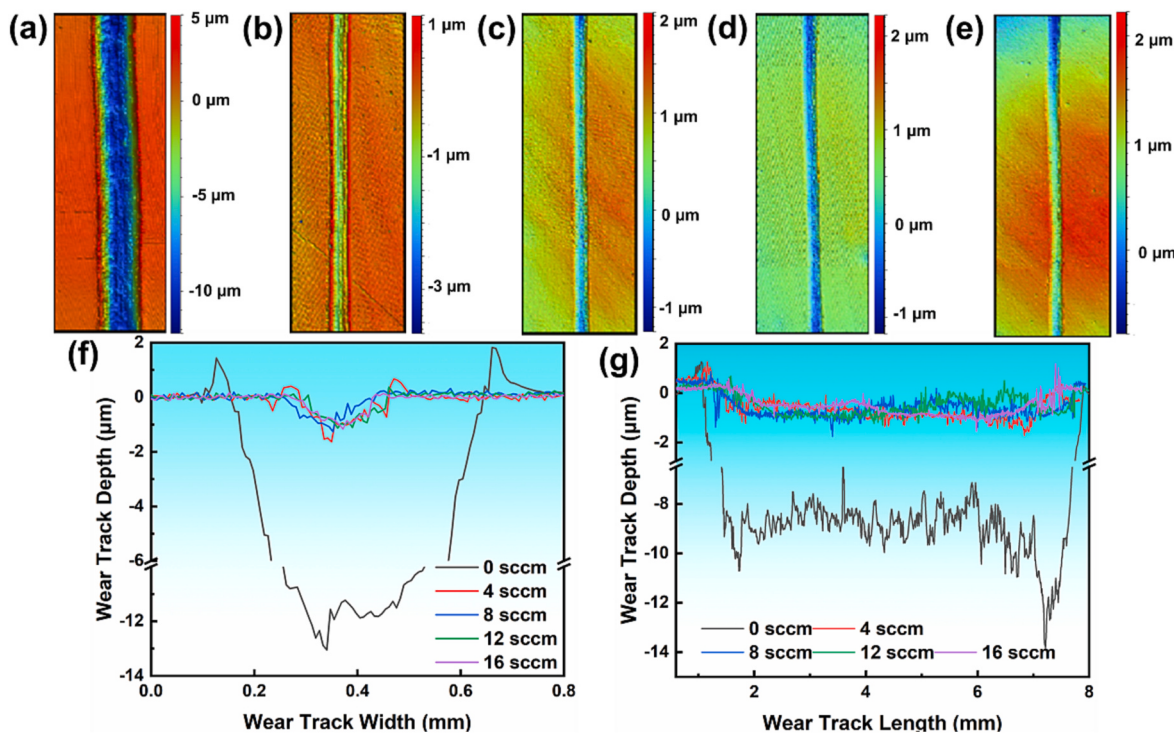
exhibits the lowest hardness, leading to more pronounced plowing grooves. In contrast, the 8, 12, and 16 sccm films, which have higher hardness, do not exhibit distinct plowing grooves, and the wear track surfaces appear relatively smoother. The mapping of the wear tracks in Fig. 12 shows that all film wear tracks exhibit the presence of oxides. This phenomenon is attributed to the generation of heat during the friction process, which causes surface oxidation in the wear tracks, leading to the presence of oxidative wear mechanisms in all films.

Fig. 13 shows the coefficients of friction and wear rates of the film at different nitrogen flows. The friction coefficient of the 0 sccm film exhibits significant fluctuations, suggesting that the film fails during friction. After the introduction of nitrogen, the friction coefficient increased and remained relatively stable for all nitride films, with minimal variations.

Fig. 14 shows the wear track profiles of the films at different nitrogen flow rates. The 0 sccm film was worn, indicating poor wear resistance. To semi-quantitatively investigate the wear resistance of the 0 sccm film, a milder friction condition, with a load of 0.5 N and GCr15 ball with a diameter of 6 mm, was selected. The wear rate was calculated to be  $1.2 \times 10^{-4} \text{ mm}^3 \text{ N}^{-1} \text{ m}^{-1}$ . The frictional conditions for the nitrogen-doped films (4, 8, 12, and 16 sccm) were maintained as follows: The sliding velocity, applied load, and frequency were kept constant at  $1.885 \text{ cm} \cdot \text{s}^{-1}$ , 2 N, and 3 Hz, respectively.  $\text{Al}_2\text{O}_3$  balls with diameters of 6 mm were used as grinding pairs. The introduction of nitrogen resulted in an increase in the wear resistance of the 4 sccm film, preventing wear-through and reducing the wear rate to  $7.79 \times 10^{-6} \text{ mm}^3 \text{ N}^{-1} \text{ m}^{-1}$ . Further increasing the nitrogen flow led to a decrease in the wear rate of the film to  $4.04 \times 10^{-6} \text{ mm}^3 \text{ N}^{-1} \text{ m}^{-1}$ . According to Archard's law [38,39], a high hardness is typically indicative of good wear resistance. Hence, the 8 sccm film outperforms the 0 and 4 sccm films. Despite the more severe friction conditions of the nitriding film, the wear rate of the 0 sccm film was still significantly high compared to that of the nitriding film. This means that the introduction of nitrogen significantly improves the wear resistance of the film. Although 12 and 16 sccm films exhibit higher hardness values, their wear rates increased slightly. The wear resistance of the film depends not only on its hardness, but also on its toughness. Liu [40] investigated the impact of Cu content on the wear resistance of NbN and found that NbN films without Cu had the highest hardness; however, their wear rates were higher than that of the NbN/Cu composite film with a Cu content of 5.2 at.%. This is because the introduction of Cu improves the toughness of the NbN film. In our study, the 8 sccm film demonstrates the best indentation toughness. This indicates that the film effectively absorbed the cracks generated during the friction deformation process, preventing large-scale peeling and failure during friction processes. Consequently, the wear resistance of the 8



**Fig. 13.** (a) Friction coefficient and (b) wear rate of the films with different nitrogen flow rates.



**Fig. 14.** (a–e) Three-dimensional and (f and g) two-dimensional contours of the film wear tracks under different nitrogen flow rates: (a) 0, (b) 4, (c) 8, (d) 12, and (e) 16 sccm.

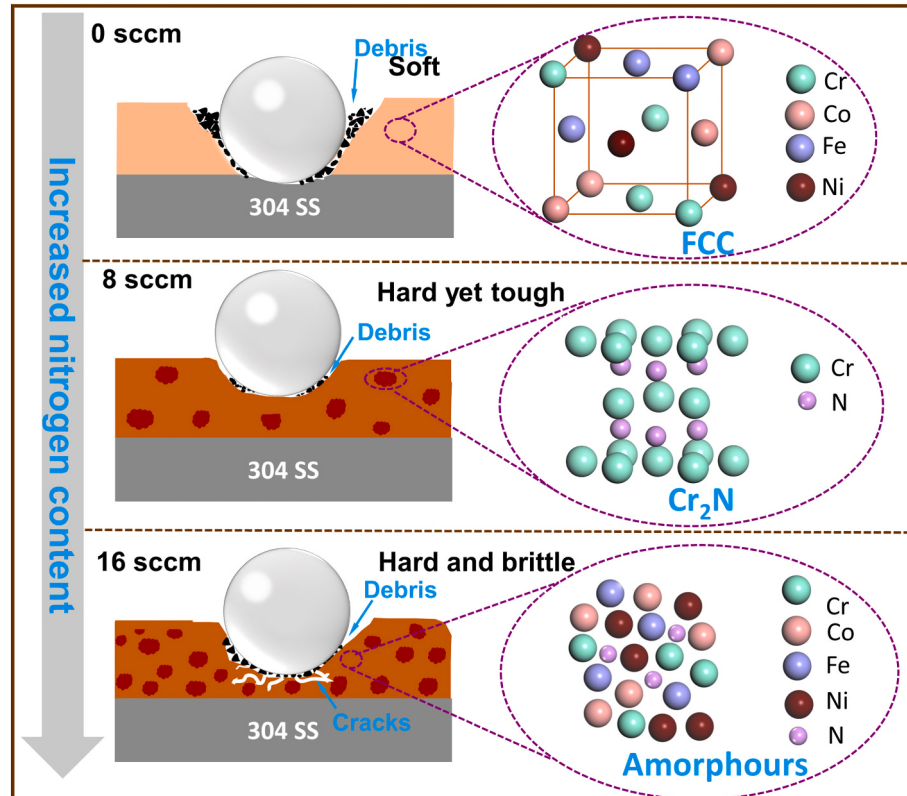


**Fig. 15.** Schematic illustration of the friction results of the FeCoNiCrN<sub>x</sub> films under different nitrogen flow rates.

sccm film was superior to those of the 12 and 16 sccm films.

Fig. 15 illustrates the influence of the nitrogen content on the structural, mechanical, and tribological properties of the films. In this

study, the tribological performance of FeCoNiCr-based films was found to depend on the coordination between hardness and toughness. The 0 sccm film exhibited a FCC structure with a higher slip system, resulting

in good plastic deformation ability but insufficient hardness, leading to poor wear resistance. When the nitrogen flow rate reaches 8 sccm, the film possessed a composite structure of amorphous and nanocrystalline phases ( $\text{Cr}_2\text{N}$ ), exhibiting both good hardness and toughness, thereby achieving the optimal wear resistance. However, as the nitrogen flow rate increases to 16 sccm, the increased ceramic phase led to higher hardness but reduced toughness, ultimately resulting in a decrease in the tribological performance.

#### 4. Conclusions

In this study, HEA films with different nitrogen contents were fabricated using reactive magnetron sputtering. The influence of the nitrogen content on the microstructure, mechanical properties, and tribological behavior of  $\text{FeCoNiCrN}_x$  HEA films was investigated. The main conclusions are as follows.

The incorporation of nitrogen atoms into the  $\text{FeCoNiCr}$  film induced film amorphization, whereas the reaction between Cr and N generated  $\text{Cr}_2\text{N}$ , resulting in the formation of a composite structure comprising amorphous and nanocrystalline phases. When the nitrogen flow rate reaches 8 sccm, the  $\text{FeCoNiCrN}$  film exhibited the best wear resistance. This can be attributed to the appropriate proportion of the metal and ceramic phases in the film. The metal phase provides good toughness, whereas the ceramic phase ensures high hardness, resulting in an optimal combination of strength and toughness, leading to favorable tribological properties. However, as the nitrogen flow rate increased further and reached saturation at 16 sccm, the excessive nitrogen content led to an increase in film hardness but a decrease in toughness, resulting in a slight deterioration in the wear resistance performance. We proposed an effective strategy to enhance and modify  $\text{FeCoNiCr}$ -based HEA films that possess good ductility but inadequate hardness. This strategy has promising application prospects in HEA films for friction protection.

#### CRediT authorship contribution statement

**W. Liu:** Writing – original draft, Validation, Methodology, Investigation. **C.T. Wang:** Methodology, Data curation. **S.C. Zhao:** Investigation, Data curation. **L. Chen:** Data curation. **Y.T. Li:** Writing – review & editing, Methodology, Data curation. **X. Jiang:** Writing – review & editing, Supervision, Resources, Project administration, Methodology, Funding acquisition, Data curation, Conceptualization. **Y.X. Leng:** Supervision, Conceptualization.

#### Declaration of competing interest

No competing financial interests or personal relationships that could have appeared to influence the work reported in this paper, and the manuscript is approved by all authors for publication. I would like to declare on behalf of my co-authors that the work described was original research that has not been published previously, and not under consideration for publication elsewhere, in whole or in part.

#### Data availability

Data will be made available on request.

#### Acknowledgment

This work was supported by the National Natural Science Foundation of China (Grant Nos. 51975564 and 52375206), the Sichuan Science and Technology Project (Grant No. 2021YFSY0050), the State Key Laboratory of Acoustics, Chinese Academy of Sciences (SKLA202214) and the Fundamental Research Funds for the Central Universities (No. 2682021CX103). We would like to thank Analysis and Testing Center of Southwest Jiaotong University for the XRD and TEM testing.

#### References

- [1] J.W. Yeh, S.K. Chen, S.J. Lin, J.Y. Gan, T.S. Chin, T.T. Shun, C.H. Tsau, S.Y. Chang, Nanostructured high-entropy alloys with multiple principal elements: novel alloy design concepts and outcomes, *Adv. Eng. Mater.* 6 (2004) 299–303, <https://doi.org/10.1002/adem.200300567>.
- [2] B. Cantor, I.T.H. Chang, P. Knight, A.J.B. Vincent, Microstructural development in equiatomic multicomponent alloys, *Mater. Sci. Eng. A* 375–377 (2004) 213–218, <https://doi.org/10.1016/j.msea.2003.10.257>.
- [3] W.H. Liu, Z.P. Lu, J.Y. He, J.H. Luan, Z.J. Wang, B. Liu, Y. Liu, M.W. Chen, C.T. Liu, Ductile  $\text{CoCrFeNiMo}_x$  high entropy alloys strengthened by hard intermetallic phases, *Acta Mater.* 116 (2016) 332–342, <https://doi.org/10.1016/j.actamat.2016.06.063>.
- [4] X. Chang, M. Zeng, K. Liu, L. Fu, Phase engineering of high-entropy alloys, *Adv. Mater.* 32 (2020), <https://doi.org/10.1002/adma.201907226>.
- [5] B. Cantor, Multicomponent high-entropy Cantor alloys, *Prog. Mater. Sci.* 120 (2021), <https://doi.org/10.1016/j.pmatsci.2020.100754>.
- [6] Y.-T. Chen, Y.-J. Chang, H. Murakami, S. Gorsse, A.-C. Yeh, Designing high entropy superalloys for elevated temperature application, *Scr. Mater.* 187 (2020) 177–182, <https://doi.org/10.1016/j.scriptamat.2020.06.002>.
- [7] J. Wang, S. Kuang, X. Yu, L. Wang, W. Huang, Tribomechanical properties of  $\text{CrNbTiMoZr}$  high-entropy alloy film synthesized by direct current magnetron sputtering, *Surf. Coat. Technol.* 403 (2020), <https://doi.org/10.1016/j.surfcoat.2020.126374>.
- [8] Y. Yan, K.A. McGarrity, D.J. Delia, C. Fekete, K. Wang, The oxidation-resistance mechanism of  $\text{WTaNbTiAl}$  refractory high entropy alloy, *Corros. Sci.* 204 (2022), <https://doi.org/10.1016/j.corsci.2022.110377>.
- [9] Y. Wang, B. Liu, K. Yan, M. Wang, S. Kabra, Y.-L. Chiu, D. Dye, P.D. Lee, Y. Liu, B. Cai, Probing deformation mechanisms of a  $\text{FeCoCrNi}$  high-entropy alloy at 293 and 77 K using in situ neutron diffraction, *Acta Mater.* 154 (2018) 79–89, <https://doi.org/10.1016/j.actamat.2018.05.013>.
- [10] C. Wang, X. Lin, L. Wang, S. Zhang, W. Huang, Cryogenic mechanical properties of 316L stainless steel fabricated by selective laser melting, *Mater. Sci. Eng. A* 815 (2021), <https://doi.org/10.1016/j.msea.2021.141317>.
- [11] T. Yang, S. Xia, S. Liu, C. Wang, S. Liu, Y. Zhang, J. Xue, S. Yan, Y. Wang, Effects of Al addition on microstructure and mechanical properties of  $\text{Al}_x\text{CoCrFeNi}$  high-entropy alloy, *Mater. Sci. Eng. A* 648 (2015) 15–22, <https://doi.org/10.1016/j.msea.2015.09.034>.
- [12] W.-R. Wang, W.-L. Wang, S.-C. Wang, Y.-C. Tsai, C.-H. Lai, J.-W. Yeh, Effects of Al addition on the microstructure and mechanical property of  $\text{Al}_x\text{CoCrFeNi}$  high-entropy alloys, *Intermetallics* 26 (2012) 44–51, <https://doi.org/10.1016/j.intermet.2012.03.005>.
- [13] Y. Tong, D. Chen, B. Han, J. Wang, R. Feng, T. Yang, C. Zhao, Y.L. Zhao, W. Guo, Y. Shimizu, C.T. Liu, P.K. Liaw, K. Inoue, Y. Nagai, A. Hu, J.J. Kai, Outstanding tensile properties of a precipitation-strengthened  $\text{FeCoNiCrTi}_{0.2}$  high-entropy alloy at room and cryogenic temperatures, *Acta Mater.* 165 (2019) 228–240, <https://doi.org/10.1016/j.actamat.2018.11.049>.
- [14] B. Chanda, J. Das, Composition dependence on the evolution of nanoeutectic in  $\text{CoCrFeNiNb}_x$  ( $0.45 \leq x \leq 0.65$ ) high entropy alloys, *Adv. Eng. Mater.* 20 (2017), <https://doi.org/10.1002/adem.201700908>.
- [15] Z. Gao, B. Sun, Y. Yu, J. Li, T. Li, L. Wang, Z. Gao, Z. Qiao, Microstructure, mechanical, and tribological properties of  $\text{CoCrFeNi-Ag-Mo}$  self-lubricating composite, *J. Mater. Eng. Perform.* (2023), <https://doi.org/10.1007/s11665-023-08085-z>.
- [16] Z. Zhang, Y. Ling, J. Hui, F. Yang, X. Zhang, S. Tan, Z. Xie, F. Fang, Effect of C additions to the microstructure and wear behaviour of  $\text{CoCrFeNi}$  high-entropy alloy, *Wear* 530–531 (2023), <https://doi.org/10.1016/j.wear.2023.205032>.
- [17] M. Song, R. Zhou, J. Gu, Z. Wang, S. Ni, Y. Liu, Nitrogen induced heterogeneous structures overcome strength-ductility trade-off in an additively manufactured high-entropy alloy, *Appl. Mater. Today* 18 (2020), <https://doi.org/10.1016/j.apmt.2019.100498>.
- [18] H. Wu, L. Wang, S. Zhang, C.L. Wu, C.H. Zhang, X.Y. Sun, J. Chen, Tribological properties and sulfuric acid corrosion resistance of laser clad  $\text{CoCrFeNi}$  high-entropy alloy coatings with different types of TiC reinforcement, *Tribol. Int.* 188 (2023), <https://doi.org/10.1016/j.triboint.2023.108870>.
- [19] Z. Gao, J. Li, L. Ke, Z. Qiao, L. Yuan, Z. Gao, C. Zhang, Microstructure and tribological properties of in-situ  $\text{M}_2\text{B}$  reinforced  $\text{CoCrFeNi}$  HEA composites prepared by laser cladding, *J. Alloys Compd.* 966 (2023), <https://doi.org/10.1016/j.jallcom.2023.171560>.
- [20] W.B. Liao, H. Zhang, Z.Y. Liu, P.F. Li, J.J. Huang, C.Y. Yu, Y. Lu, High strength and deformation mechanisms of  $\text{Al}_{0.3}\text{CoCrFeNi}$  high-entropy alloy thin films fabricated by magnetron sputtering, *Entropy* 21 (2019), <https://doi.org/10.3390/e21020146>.
- [21] W. Liao, S. Lan, L. Gao, H. Zhang, S. Xu, J. Song, X. Wang, Y. Lu, Nanocrystalline high-entropy alloy ( $\text{CoCrFeNiAl}_{0.3}$ ) thin-film coating by magnetron sputtering, *Thin Solid Films* 638 (2017) 383–388, <https://doi.org/10.1016/j.tsf.2017.08.006>.
- [22] S.R. Oh, K. Yao, C.L. Chow, F.E.H. Tay, Residual stress in piezoelectric poly(vinylidene-fluoride-co-trifluoroethylene) thin films deposited on silicon substrates, *Thin Solid Films* 519 (2010) 1441–1444, <https://doi.org/10.1016/j.tsf.2010.09.042>.
- [23] B. Liu, J. Wang, Y. Liu, Q. Fang, Y. Wu, S. Chen, C.T. Liu, Microstructure and mechanical properties of equimolar  $\text{FeCoCrNi}$  high entropy alloy prepared via powder extrusion, *Intermetallics* 75 (2016) 25–30, <https://doi.org/10.1016/j.intermet.2016.05.006>.
- [24] Z. He, N. Jia, H. Yan, Y. Shen, M. Zhu, X. Guan, X. Zhao, S. Jin, G. Sha, Y. Zhu, C. T. Liu, Multi-heterostructure and mechanical properties of N-doped  $\text{FeMnCoCr}$

- high entropy alloy, *Int. J. Plast.* 139 (2021) 102965, <https://doi.org/10.1016/j.ijplas.2021.102965>.
- [25] D.E. Jodi, J. Park, B. Straumal, N. Park, Investigation on the precipitate formation and behavior in nitrogen-containing equiatomic CoCrFeMnNi high-entropy alloy, *Mater. Lett.* 258 (2020) 126806, <https://doi.org/10.1016/j.matlet.2019.126806>.
- [26] D.E. Jodi, J. Park, N. Park, Precipitate behavior in nitrogen-containing CoCrNi medium-entropy alloys, *Mater Charact* 157 (2019) 109888, <https://doi.org/10.1016/j.matchar.2019.109888>.
- [27] M.C. Biesinger, B.P. Payne, A.P. Grosvenor, L.W.M. Lau, A.R. Gerson, R.S.C. Smart, Resolving surface chemical states in XPS analysis of first row transition metals, oxides and hydroxides: Cr, Mn, Fe, Co and Ni, *Appl. Surf. Sci.* 257 (2011) 2717–2730, <https://doi.org/10.1016/j.apsusc.2010.10.051>.
- [28] A. Lippitz, T. Hübner, XPS investigations of chromium nitride thin films, *Surf. Coat. Technol.* 200 (2005) 250–253, <https://doi.org/10.1016/j.surfcoat.2005.02.091>.
- [29] C. Han, X. Xu, H. Mu, Q. Tian, Q. Li, Y. Liu, X. Zhang, Z. Zhao, X. Su, Construction of hierarchical sea urchin-like manganese substituted nickel cobaltite@tricobalt tetraoxide core-shell microspheres on nickel foam as binder-free electrodes for high performance supercapacitors, *J. Colloid Interface Sci.* 596 (2021) 89–99, <https://doi.org/10.1016/j.jcis.2021.03.131>.
- [30] S. Liu, W. Qi, J. Liu, X. Meng, S. Adimi, J.P. Attfield, M. Yang, Modulating electronic structure to improve the solar to hydrogen efficiency of cobalt nitride with lattice doping, *ACS Catal.* 13 (2023) 2214–2222, <https://doi.org/10.1021/acscatal.2c05075>.
- [31] Y. Dong, B. Wang, K. Zhao, Y. Yu, X. Wang, L. Mai, S. Jin, Air-stable porous Fe<sub>2</sub>N encapsulated in carbon microboxes with high volumetric lithium storage capacity and a long cycle life, *Nano Lett.* 17 (2017) 5740–5746, <https://doi.org/10.1021/acs.nanolett.7b02698>.
- [32] J.-T. Ren, Y.-S. Wang, Y.-J. Song, L. Chen, Z.-Y. Yuan, Interface engineering of in-situ formed nickel hydr(oxy)oxides on nickel nitrides to boost alkaline hydrogen electrocatalysis, *Appl. Catal. B* 309 (2022) 121279, <https://doi.org/10.1016/j.apcatb.2022.121279>.
- [33] A. Takeuchi, A. Inoue, Classification of bulk metallic glasses by atomic size difference, heat of mixing and period of constituent elements and its application to characterization of the main alloying element, *Mater. Trans.* 12 (2005) 46, <https://doi.org/10.2320/matertrans.46.2817>.
- [34] N.A. Khan, B. Akhavan, C. Zhou, H. Zhou, L. Chang, Y. Wang, Y. Liu, M.M. Bilek, Z. Liu, High entropy nitride (HEN) thin films of AlCoCrCu<sub>0.5</sub>FeNi deposited by reactive magnetron sputtering, *Surf. Coat. Technol.* 402 (2020) 126327, <https://doi.org/10.1016/j.surfcoat.2020.126327>.
- [35] C.-Y. Lu, W. Diyatiwika, B.-S. Lou, Y.-C. Lu, J.-G. Duh, J.-W. Lee, Influences of target poisoning on the mechanical properties of TiCrBN thin films grown by a superimposed high power impulse and medium-frequency magnetron sputtering, *Surf. Coat. Technol.* 332 (2017) 86–95, <https://doi.org/10.1016/j.surfcoat.2017.06.081>.
- [36] S. Veprek, A. Niederhofer, K. Moto, T. Bolom, H.-D. Männling, P. Nesladek, G. Dollinger, A. Bergmaier, Composition, nanostructure and origin of the ultrahardness in nc-TiN/a-Si<sub>3</sub>N<sub>4</sub>/a- and nc-TiSi<sub>2</sub> nanocomposites with HV = 80 to  $\geq$ 105 GPa, *Surf. Coat. Technol.* 133–134 (2000) 152–159, [https://doi.org/10.1016/S0257-8972\(00\)00957-9](https://doi.org/10.1016/S0257-8972(00)00957-9).
- [37] W. Yu, W. Li, P. Liu, K. Zhang, F. Ma, X. Chen, R. Feng, P.K. Liaw, Silicon-content-dependent microstructures and mechanical behavior of (AlCrTiZrMo)-Si<sub>x</sub>N high-entropy alloy nitride films, *Mater. Des.* 203 (2021) 109553, <https://doi.org/10.1016/j.matdes.2021.109553>.
- [38] Y.S. Chai, I.I. Argatov, Fretting wear accumulation in partial-slip circular Hertzian contact, *Mech. Res. Commun.* 96 (2019) 45–48, <https://doi.org/10.1016/j.mechrescom.2019.02.005>.
- [39] Y. Zhou, C. Zhu, B. Gould, N.G. Demas, H. Liu, A.C. Greco, The effect of contact severity on micropitting: simulation and experiments, *Tribol. Int.* 138 (2019) 463–472, <https://doi.org/10.1016/j.triboint.2019.06.020>.
- [40] J. Liu, C. Liang, The improvement of toughness and tribological properties of niobium nitride film by addition of copper, *Vacuum* 143 (2017) 59–62, <https://doi.org/10.1016/j.vacuum.2017.05.040>.